Dielectronic recombination of heliumlike ions

D. A. Knapp, R. E. Marrs, M. B. Schneider, M. H. Chen, M. A. Levine,*
and P. Lee†
Physics Department, Lawrence Livermore National Laboratory, Livermore, California 94550
(Received 21 September 1992)

We have measured $\Delta n \geq 1$ dielectronic-recombination cross sections for the heliumlike ions Ni^{26+}, Mo^{40+}, and Ba^{54+}. We observed the x rays emitted during dielectronic recombination by ions in an electron-beam ion trap and obtained cross sections from a calibration based upon radiative recombination. The results generally agree well with theoretical predictions.

PACS number(s): 34.80.Kw, 32.80.Hd, 52.25.Nr

I. INTRODUCTION

Dielectronic recombination, the resonant capture of electrons by ions, is an important process in plasmas. It strongly affects both the ionization balance of a plasma and its emitted x-ray spectrum. It also serves as a valuable benchmark for atomic-physics calculations because of its sensitivity to both the Auger and radiative decay rates of doubly excited atomic states.

We have measured $\Delta n \geq 1$ dielectronic-recombination cross sections in three heliumlike ions with a wide range of atomic numbers: Ni^{26+}, Mo^{40+}, and Ba^{54+}. The ions were created, ionized, and trapped in an electron-beam ion trap. We observed dielectronic recombination by detecting the characteristic x rays emitted in the process, using the photons emitted by radiative recombination to calibrate the cross sections.

These measurements use an improved technique similar to that used for our previously reported results on Ni^{26+} [1] and neonlike ions [2].

II. DIELECTRONIC-RECOMBINATION THEORY

Dielectronic recombination is the resonant capture of a free electron by an ion via an intermediate doubly excited state. Schematic diagrams of some relevant atomic processes are shown in Fig. 1. In the nonresonant process of radiative recombination (RR), an ion captures an electron into a vacant bound state, emitting a photon with an energy equal to the electron's initial kinetic energy plus the binding energy of its final atomic state:

$$\text{RR}: \ A^{q+} + e^- \rightarrow A^{(q-1)+} + \gamma.$$

If the recombination energy is equivalent to the excitation energy of a doubly excited state in the recombined ion, a nonradiative resonant time-reversed Auger process may occur. This process leaves the ion in an intermediate state with both the recombined electron and a previously unexcited electron in excited states. The intermediate doubly excited state will decay either radiatively or by Auger emission. In the latter process, emission of an Auger electron, the system usually goes back to the initial energy state, in which case the entire process amounts to resonant elastic scattering (RS):

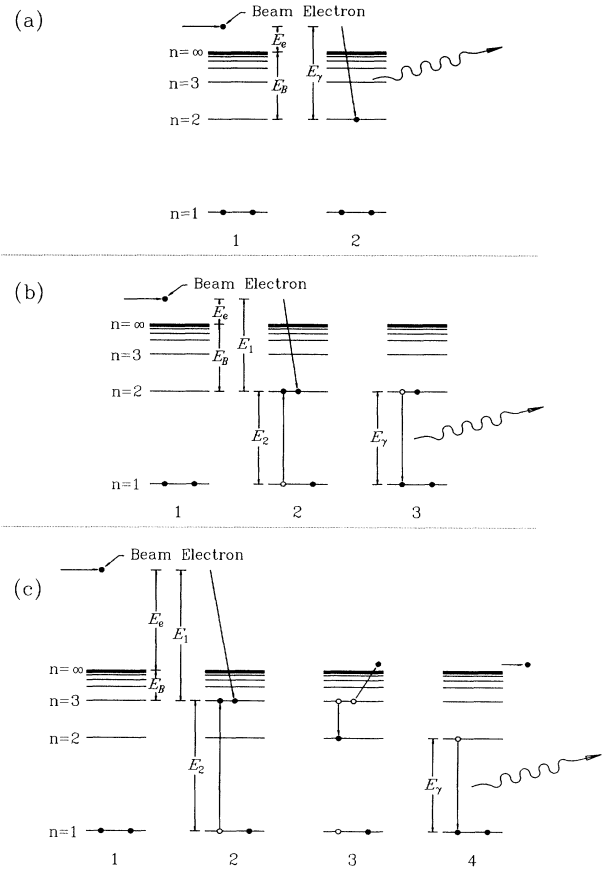

FIG. 1. Illustration of dielectronic recombination. (a) Radiative recombination. A beam electron is captured into a vacant orbital of an ion, and a photon is emitted. The energy of the photon E_γ is equal to the initial electron energy E_e plus the binding energy of the final state E_B. (b) Dielectronic recombination. If $E_1 = E_2$, a beam electron may be resonantly captured into a bound state while exciting another electron already present in the ion (2). If the resulting doubly excited intermediate state decays radiatively (3), the process is dielectronic recombination. (c) Resonant excitation. The resonant doubly excited state decays by Auger emission (3), leaving the ion in an excited state, which subsequently radiatively decays (4).

$$\text{RS}: \; A^{q+} + e^- \rightarrow [A^{(q-1)+}]^{**} \rightarrow A^{q+} + e^-.$$

If the Auger decay proceeds to a bound atomic state different from the initial state, the resulting excited state will decay radiatively, resulting in resonant excitation (RE):

$$\text{RE}: \; A^{q+} + e^- \rightarrow [A^{(q-1)+}]^{**} \rightarrow [A^{q+}]^* + e^- \rightarrow A^{q+} + e^- + \gamma.$$

If the doubly excited intermediate state decays radiatively to a bound state the process is known as dielectronic recombination (DR):

$$\text{DR}: \; A^{q+} + e^- \rightarrow [A^{(q-1)+}]^{**} \rightarrow A^{(q-1)+} + n\gamma.$$

Dielectronic-recombination and resonant-excitation resonances are usually labeled using the notation for the inverse Auger process; for example, the KLL dielectronic-recombination resonance is one in which a continuum electron is captured to the L shell, while a K-shell electron is excited to the L shell. $\Delta n \geq 1$ dielectronic-recombination resonances are those for which the excited bound electron changes principal quantum number.

The resonance strength for an isolated DR resonance is expressed in terms of the Auger and radiative widths of the doubly excited intermediate state:

$$S_{d\rightarrow f} \equiv \int_{-\infty}^{\infty} \sigma_{d\rightarrow f}(E)dE = \frac{2\pi^2}{k_i^2} \frac{A_A(i\rightarrow d)\, A_r(d\rightarrow f)}{\sum A_A + \sum A_r}, \quad (1)$$

where i, d, and f refer to the initial, intermediate doubly excited, and final states, respectively, $A_A(i \rightarrow d) = g_d/2g_i A_A(d\rightarrow i)$ is the width for inverse Auger capture to the resonant state, $A_r(d\rightarrow f)$ is the partial width of state d for radiative transition to state f, $\sum A_A$ and $\sum A_r$ are the total Auger and radiative widths of the intermediate state, g_i and g_d are the statistical weights for the initial and intermediate states, and k_i is the wave number of the incident electron. The energy width of $\Delta n \geq 1$ dielectronic-recombination resonances is generally so small compared to any instrumental resolution that the resonances can be treated as δ functions with an area equal to $S_{d\rightarrow f}$.

III. APPARATUS AND METHOD

A. The EBIT

We performed our measurements of dielectronic recombination with the electron-beam ion trap (EBIT) at the Lawrence Livermore National Laboratory. This device, described in detail in previous papers [3,4], produces and traps highly charged ions. The trap consists of a magnetically compressed electron beam passing through a series of three drift tubes. The space charge of the electron beam traps the ions radially, while potentials applied to the end drift tubes form the axial trap. The trap typically confines approximately 4×10^4 high-charge ions in a volume approximately 60 μm in diameter and 2 cm long. In addition to trapping the ions, the electron beam also serves to ionize and excite them. A simplified schematic of the trap is shown in Fig. 2, and a summary of EBIT operating parameters is given in Table I.

The electron-beam energy in the trap is controlled by the potential of the central drift tube. The EBIT electron-gun cathode is at ground potential, so the electron-beam energy in the central drift tube is equal to the voltage applied to the drift tube minus the space-charge potential of the beam. Since the ions in the trap have very low kinetic energies, typically about $20q$ eV, the electron-ion interaction energy is essentially equivalent to the electron-beam energy. The beam electrons have a narrow energy distribution, typically 50–70-eV full width at half maximum (FWHM). The electron-ion interaction rate and plasma density are both sufficiently low to ensure a negligible population of metastable atomic states.

The energy imparted to the high-charge ions by the electron-ion collisions heats the ions. We remove this energy by means of "evaporative cooling," in which low-Z, low-charge ions continuously escape from the trap, cooling the high-charge ions [4]. This process results in long trapping times for high-Z ions. For these measurements, the low-Z ions were formed from neutral N_2 gas injected continuously into the trap. The cooling process concentrates high-Z contaminants in the trap, especially barium (Z=56) evaporated from the cathode of the electron gun. This effect limits useful trapping times for light ions. Ion-trapping times in the EBIT range from a few seconds for $Z<22$ to several hours for $Z>70$.

The x rays emitted by the ions in the trap are viewed at 90° to the electron-beam direction by a 200 mm^2 $\times$ 1.0 cm thick hyperpure germanium (HPGe) detector through a slot in the center drift tube. The detector was located 17 cm from the center of the trap, thus covering a solid angle of about 5.5×10^{-4} of 4π sr.

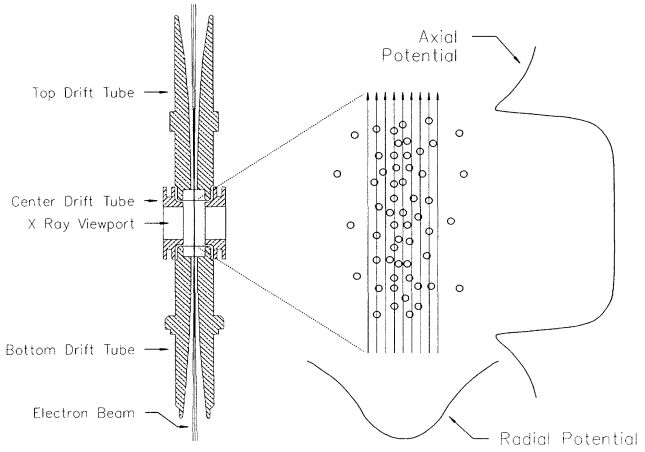

FIG. 2. The electron-beam ion trap (EBIT). Ions are trapped radially in a high-current-density electron beam by the space charge of the beam, and axially by voltage applied to drift tubes. The electron beam traps, ionizes, and excites the ions.

TABLE I. EBIT operating parameters for the dielectronic-recombination experiments.

Parameter	Symbol	Value
Beam energy	E_B	4–30 keV
Beam current	I_B	70–150 mA
Beam current density	j_e	2500–5000 A/cm^2
Beam radius in trap	r_B	30 μm
Trap length		2 cm
Visible trapped ions	N_q	4×10^4

For the dielectronic-recombination measurements, low-charge Ni and Mo ions were injected into the trap from a metal-vapor vacuum-arc (MEVVA) source [5]; the Ba ions were formed from neutral Ba atoms evaporated from the cathode of the electron gun and ionized in the electron beam.

B. Data acquisition

A schematic diagram of the data-taking scheme for dielectronic-recombination measurements is shown in Fig. 3. After injection, we raised the drift-tube voltage (and thus the electron-beam energy) from the value required for injection to an energy chosen to generate the desired ionization-state distribution. For heliumlike ions, this corresponds to an energy just below the ionization threshold. After a delay to allow the ionization balance to reach equilibrium, data acquisition commenced. During this phase, the beam energy swept linearly from the ionization energy through the dielectronic-recombination resonances and back. The beam energy stayed at the ionization energy between sweeps to maintain the ionization balance. The detection of an x ray during the energy sweep triggered the data-acquisition electronics. For each event, the system recorded the x-ray energy, beam energy, and event time.

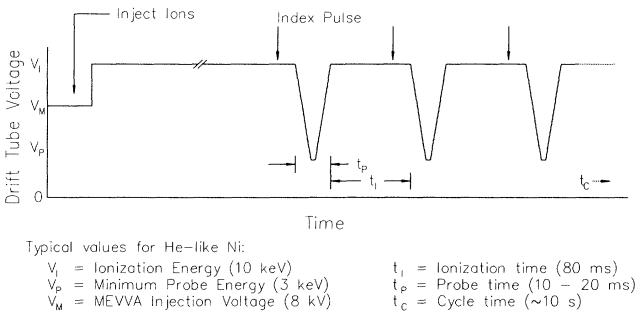

FIG. 3. Timing diagram for dielectronic-recombination measurements with the EBIT. The ions are injected with the drift tubes at the injection voltage V_M. The beam energy is then raised to generate the required ionization balance by raising the drift-tube voltage to V_I. After the ionization balance has come to equilibrium, the beam energy is swept through the dielectronic-recombination resonances and back again. The number of sweeps per injection depends upon the ions being investigated.

This "event-mode" data-acquisition scheme has several advantages. First, the energy sweep may be performed quickly to prevent significant ionization-state depletion from recombination during the measurement. Second, this method allows the sampling of a wide range of electron-beam energies with the same ions, with no need for internal normalization. Third, the method allows simultaneous observation of all electron-ion interactions that result in photon emission.

For these measurements, the energy sweeps were performed in a few tens of msec. During the sweeps, the electron-beam current was reduced from 150 to 70 mA to decrease the beam energy width and to reduce recombination. The number of sweeps per injection varied depending on the trapping time and data rate for the ion species being studied. The sweep was generated by a HP 3314A programmable function generator. This model provides programmable voltage vectors, as opposed to point-to-point digital programmability, a factor important for these measurements. The beam energy was monitored by measuring the voltage across the feedback resistor in the drift-tube high-voltage regulator. The capacitance of the drift-tube structure resulted in a delay between the measured voltage and the actual drift-tube voltage. The linearity of the voltage sweep ensures that this time delay only results in a simple offset from the true voltage, while a nonlinear sweep (such as the stepping that occurs from a digitally programmable wave-form generator) could result in a more complicated effect and reduced energy resolution.

The ionization energies used for the Ni and Mo data were just below the respective ionization energies for the heliumlike ions (10 and 21 keV, respectively). However, the maximum available drift-tube voltage in the EBIT limited the energy range for the Ba data, so the ioniza-

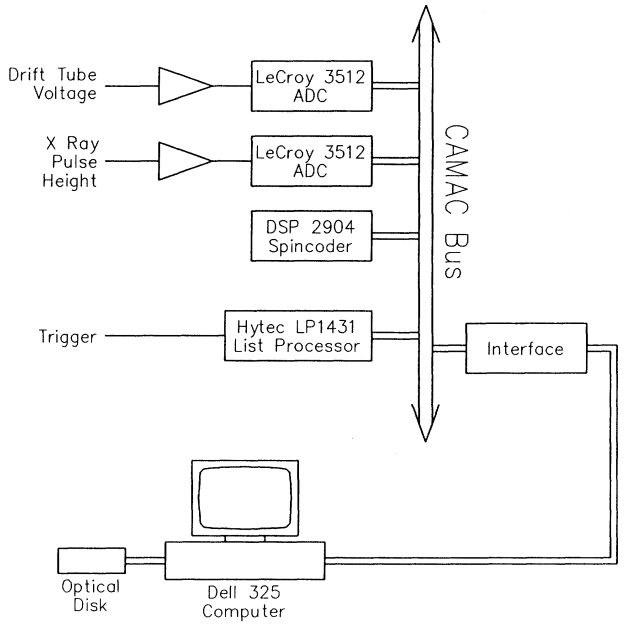

FIG. 4. Simplified schematic of the data-acquisition system.

tion energy was set to about 28 keV, and only the KLL resonances were observed.

The data-acquisition system layout is shown in Fig. 4. The voltages were digitized by 13-bit LeCroy 3512 analog-to-digital converters (ADC's) and the time reported by a DSP 2904 spincoder-timer with a resolution of 1.6 μs. The values for each event were read through a computer-aided measurement-and-control bus (CAMAC) by a Hytec LP1431 list processor and saved in local memory. This system provided a low fixed acquisition dead time of 30 μs per event. At the end of an EBIT timing cycle, during injection and initial ionization of a new set of ions, the accumulated data were sent to a Dell 325 computer and stored. A test pulser generated an "index" event prior to each beam energy sweep, providing a time fiducial and gain stabilization.

IV. ANALYSIS

A. Data

Typical raw data are shown as a scatter plot of x-ray energy vs electron-beam energy in Fig. 5. Each process responsible for emission of x rays produces a unique signature: bound-state–bound-state transitions form vertical lines, radiative-recombination photons form angled lines (since their energy equals the beam energy plus the binding energy of the recombined state), and dielectronic recombination and resonant excitation form intense spots.

We generated excitation functions for x-ray emission by applying cuts to the data, as illustrated in Fig. 5, selecting the events of interest, and projecting these events onto the beam energy axis. A diagonal window allows selection of photons produced by radiative recombination to the n=2 shell, while a vertical window selects the x rays from n=2-1 bound-state–bound-state transitions. Excitation functions generated from these cuts are shown in Fig. 6.

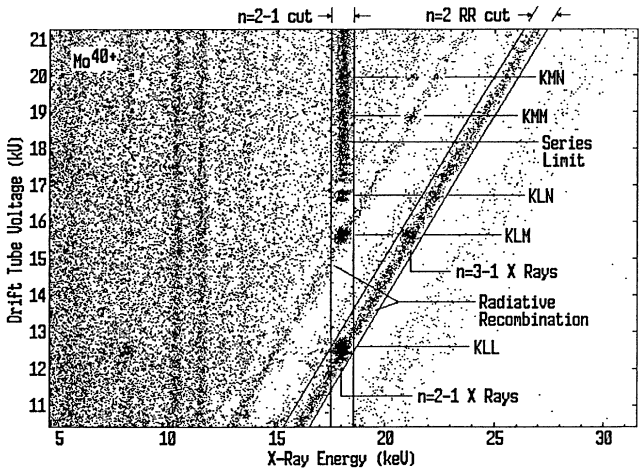

FIG. 5. Scatter plot of observed events for Mo^{40+}. x axis is x-ray energy, and y axis is electron-beam energy. Different electron-ion processes leave distinctive signatures in this plot. The windows used for cuts to select data around the n=2-1 x-ray line and the n=2 radiative-recombination photons are shown.

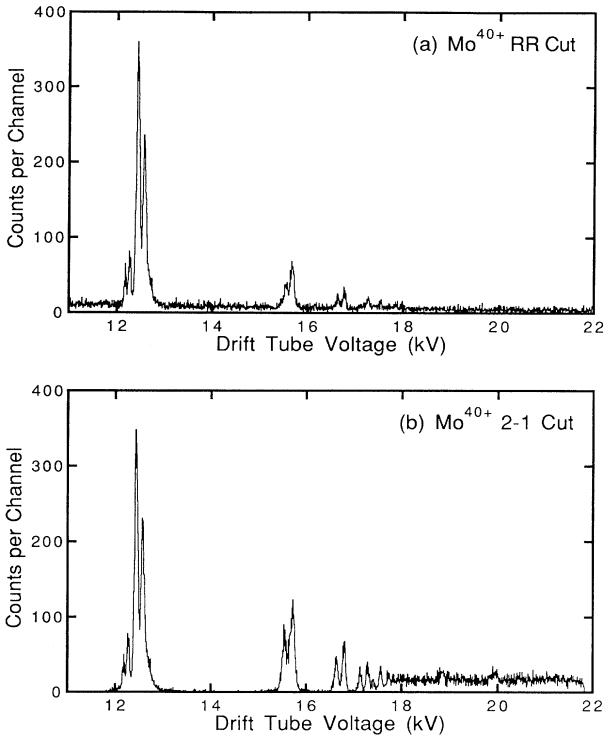

FIG. 6. Excitation functions for different cuts of the Mo^{40+} data. The radiative-recombination photons appear as a continuum under the dielectronic-recombination resonances in the n=2 radiative-recombination cut.

The small time delay between the actual beam energy and the recorded energy prevented direct combination of the data from the down-going and up-going portions of the sweep. Instead, the down-going and up-going data were compared to identify any effects from dead time or ionization-balance changes during the sweep. No difference was observed between the down-going and up-going excitation functions.

B. Ionization balance variation

During a single sweep of the electron-ion interaction energy across a dielectronic-recombination resonance with resonance strength S, the fraction of ions that recombine is

$$\frac{\Delta N_q}{N_q} = -\langle j_e \rangle S \frac{dt}{dE}, \tag{2}$$

where $\langle j_e \rangle$ is the effective current density and dE/dt is energy sweep rate. The high sweep rates used in our measurements permitted only minimal recombination, a significant advantage over fixed-energy measurements. A single ionization balance applies to the full range of interaction energies, making calibration of the cross-section scale much less subject to systematic errors. Table II shows the energy sweep rates and the maximum expected recombination fractions, using theoretical dielectronic-recombination resonance strengths and assuming a perfect ion-beam overlap. The listed values do not include

TABLE II. Predicted recombination fractions during voltage sweeps across dielectronic resonances in one direction. The Ba value is for the KLL resonances only.

	Ni^{26+}	Mo^{40+}	Ba^{54+}
Sweep rate	-0.553 eV/μs	-1.18 eV/μs	-0.112 eV/μs
$-\Delta N_{He}/N_{He}$	4.2%	1.2%	4.4%

the effects of ionization and radiative-recombination during the sweep, but these effects can safely be ignored since they are relatively small and largely cancel.

C. Dead-time corrections

The data-acquisition system dead time has a markedly different effect for these data than that usually observed in counting experiments. Each observed event casts a "shadow" over the interaction energies immediately following it in the sweep. This effect was verified by an experiment in which a test pulse was generated at a fixed time in the energy sweep, and the resulting time gap in otherwise random data measured. The dead-time correction for each electron energy in the data was computed by integrating the observed data rate over the previous 30 μs, the (fixed) dead time of the data-acquisition system. At the maximum event rate of 2000 sec^{-1}, observed in the Ni data, the dead-time correction amounted to only about 6%.

D. Calibration of cross sections to radiative recombination

We obtained the dielectronic-recombination cross sections by calibration to the radiative-recombination intensity. The radiative-recombination cross sections can be calculated to a theoretical accuracy better than about 3% [6], and have been confirmed experimentally by measurements of photoionization cross sections. The calibration procedure consisted of fitting data from a cut around the n=2 radiative-recombination photons. This cut included x rays from several dielectronic-recombination resonances, including the n=2-1 x rays from the KLL resonance, the n=3-1 x rays from the KLM resonance, etc.

The data were fitted to a function consisting of the predicted relative dielectronic-recombination resonance strengths and predicted radiative-recombination cross sections for each ionization state. The predicted amplitude of the excitation function is given by

$$F(E) = \epsilon(E)\, C(E) \sum_q W_q \left\{ \frac{d\sigma_{RR}(q,E')}{d\Omega} + K \left[\sum_{d,f} \frac{S_{d\to f}\, P_{d\to f}(90°)}{4\pi\sqrt{2\pi}} \exp\left(\frac{-(E'-E_d)^2}{2W_B^2} \right) \right] \right\}, \tag{3}$$

where W_q is the fraction of the ions in ionization state q, S_d is the dielectronic-recombination resonance strength for resonance d, E_d is the resonance energy, $E' = V_{DT} - E_0$ is the electron-ion interaction energy corrected for the energy offset between the drift-tube voltage V_{DT} and the beam energy, W_B is the electron-beam energy width, $P_{d\to f}(90°) = 1 - \beta_{d\to f}/2$ is a factor that describes the anisotropic distribution of the dielectronic-recombination radiation in terms of an angular anisotropy factor $\beta_{d\to f}$ [7], $d\sigma_{RR}(q,E')/d\Omega$ is the differential n=2 radiative-recombination cross section at 90°, and $\epsilon(E)$ is the detector efficiency. $C(E)$ is the calibration factor to transform counts per channel into a differential cross section, parametrized as

$$C(E) = c_1(1 + c_2 E), \tag{4}$$

and K is an independent amplitude factor for the dielectronic recombination. K=1 implies that the observed cross sections agree perfectly with the theoretical cross sections. The fitted parameters are c_1, c_2, W_q, K, E_0, and W_B.

Because of the small number of counts per channel in the n=2 radiative recombination, we used the Poisson maximum-likelihood estimator Ξ^2 for the fits [8, 9]. This estimator ensures that the area of the fit is equal to the area of the data, providing unbiased estimates of the fit parameters, particularly (in this case) the cross-section calibration.

In essence, the shape of the KLL dielectronic-recombination resonances determined the estimate of the ionization balance, because the resonances for the different ionization states are resolved, while the magnitude of

TABLE III. Total theoretical dielectronic-recombination resonance strengths in cm^2 eV for heliumlike ions.

Resonance group	Ni^{26+}	Mo^{40+}	Ba^{54+}
KLL	6.72×10^{-19}	4.53×10^{-19}	3.15×10^{-19}
KLM	3.99×10^{-19}	2.30×10^{-19}	
KLN	1.71×10^{-19}	9.35×10^{-20}	
KLO	8.82×10^{-20}	4.65×10^{-20}	
KLn (n=6–14)	1.54×10^{-19}	7.90×10^{-20}	

TABLE IV. Parameters from fits to the KLL resonances for the ion species studied.

Parameter	Symbol	Ni^{26+}	Mo^{40+}	Ba^{54+}
Estimator	Ξ^2	383.0	363.2	334.9
Degrees of freedom		286	351	312
Beam energy width	W_B	30.9 eV	27.1 eV	26.0 eV
Relative to theory	K	0.8308	1.0177	1.0001
Heliumlike fraction	A_{He}	89.56%	72.01%	30.11%
Lithiumlike fraction	A_{Li}	6.75%	22.28%	42.99%
Berylliumlike fraction	A_{Be}	0.31%	4.41%	23.76%
Boronlike fraction	A_B	<.1%	1.30%	3.143%

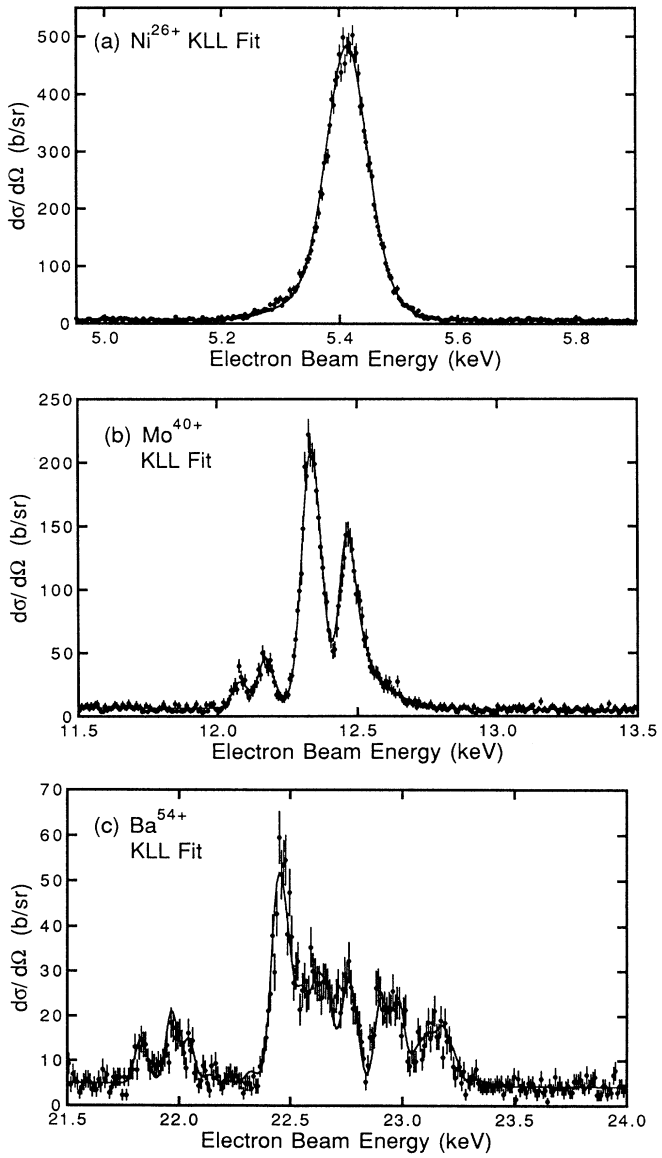

FIG. 7. Fits to the KLL resonances in the $n = 2$ radiative-recombination cuts for (a) Ni, (b) Mo, and (c) Ba ions. See Table IV for the relevant fit parameters.

the radiative recombination determined the cross-section scale. We used only data in the energy region around the KLL resonances to determine the ionization balance because these resonances provide the greatest sensitivity.

Although it may seem that using the shape of the KLL excitation function to determine the KLL cross section is circular, the procedure is actually quite robust. It is immune to overall errors in the theoretical dielectronic-recombination resonance strengths; if they are all in error by a constant factor, the cross-section scale will be unaffected. If the relative theoretical amplitudes of the resonances are in error, then the cross-section scale will be affected, but this effect will be relatively small. The n=2 radiative-recombination cross sections do not vary dramatically with ionization state, making the cross-section scale insensitive to errors in the ionization balance. Additionally, the nonheliumlike fractions for the Ni and Mo measurements were small, so any errors in the ionization balance are proportionally smaller. For the Ba data, the dielectronic-recombination resonances are well resolved in electron energy, reducing the possibility of systematic error.

The sensitivity to such errors was evaluated quantitatively for the Mo data. The relative theoretical KLL resonance strengths used in the fit were modified by dividing every other resonance strength by a factor of 2. The Mo data were then refit using these modified resonance strengths and a cross-section scale obtained. The resulting error in the cross-section scale was 4.9%.

The theoretical dielectronic-recombination resonance strengths were calculated according to (1), with the detailed Auger and radiative rates computed using a multiconfiguration Dirac-Fock code [10]. The resonances

TABLE V. Uncertainties in the cross-section scales.

Source of uncertainty	Ni^{26+}	Mo^{40+}	Ba^{54+}
Statistical	0.4%	2.3%	2.2%
DR theory	2.5%	2%	1.5%
RR theory	3%	3%	3%
RR contamination	1%		
Recombination during sweep	2%	0.5%	2%
Total	8%	8%	8%

were treated as δ functions normalized to the energy-averaged cross sections [11]. The computed total resonance strengths for the observed resonance groups are given in Table III. The anisotropic angular distributions of the stabilizing radiation were included in the theoretical predictions of the experimental observations [7], so our results are presented as differential cross sections at 90°.

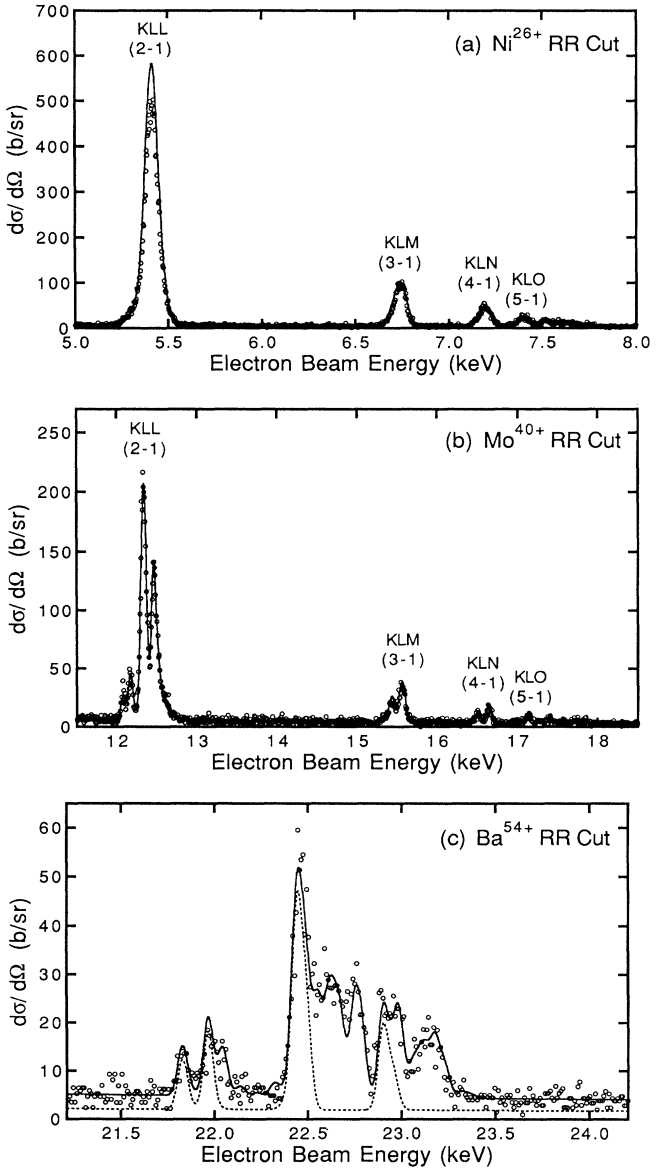

FIG. 8. Observed excitation cross sections along the n=2 radiative-recombination line for (a) Ni, (b) Mo, and (c) Ba ions. The cross sections given are for radiative stabilization from the higher n electron, e.g., the n=2-1 transitions for the KLL resonances, the n=3-1 transitions for the KLM resonances, etc. The solid lines in these plots are the theoretical resonance strengths for these transitions plus the radiative-recombination cross sections convoluted with the ionization balances and beam energy widths from the fits to the shapes of the KLL resonances. The broken line in (c) includes only the heliumlike ionization state.

V. RESULTS

The fits around the KLL resonances for the three ion species studied are shown in Fig. 7. The parameters of interest for these fits are given in Table IV. Using the ionization balance and electron-beam energy width from these fits, and cross-section scale parameters derived from the radiative recombination at energies between dielectronic-recombination resonances, the theoretical predictions were extrapolated along the n=2 radiative-recombination line and along the n=2-1 x-ray line. The results are shown in Figs. 8 and 9. For the n=2 radiative-recombination cut, the x rays included for each resonance were those with energies approximately equal to the n=2 radiative-recombination photons; thus, for the KLL resonances the n=2-1 x rays were measured; for the KLM resonances, the n=3-1 x rays, etc. For the n=2-1 cut, only the n=2-1 x rays were included. As can be seen from Fig. 5, these two branches make up most of the dielectronic-recombination stabilizing radiation. Our ability to separate the different stabilizing transitions re-

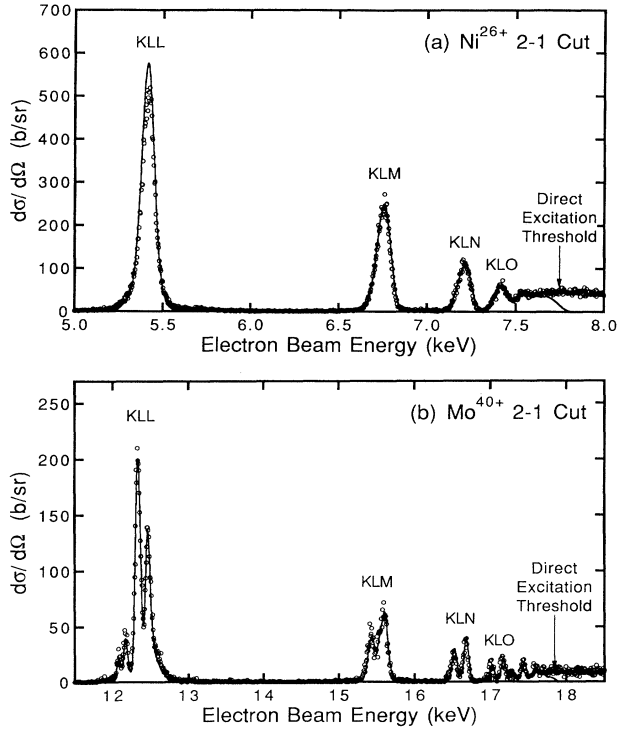

FIG. 9. Observed excitation cross sections for n=2-1 x rays for (a) Ni and (b) Mo ions. The solid lines are the theoretical dielectronic resonance strengths for n=2-1 transitions transformed as described in Fig. 8.

sults in a more stringent test of theoretical predictions than does measurement of the total cross section at each energy.

The uncertainty of the cross-section scale is made up of several factors, summarized in Table V. The uncertainty from the use of theoretical resonance strengths to obtain the ionization balance was estimated from the effect of using grossly incorrect relative resonance strengths, as described above. The theoretical uncertainty in the calculation of the differential radiative-recombination cross sections is conservatively estimated at 3%. The Ni n=2 radiative recombination had a small contamination from neonlike Ba n=3 radiative recombination. We determined its relative magnitude (about 4%) by fitting the radiative-recombination lines in the x-ray spectrum obtained at the ionization energy between voltage sweeps.

The Ni^{26+} cross sections are consistent with our earlier measurements [1]; however, the theoretical predictions in that paper assumed isotropic radiation. The agreement between observation and the corrected theory for the KLL resonances is now somewhat worse. However, the agreement between the corrected theoretical predictions and the other Ni^{26+} resonances, the Mo^{40+} results, and the Ba^{54+} results is excellent.

VI. SUMMARY

We have developed a useful and versatile method to measure dielectronic-recombination cross sections, and have used it to measure the $\Delta n \geq 1$ cross sections for heliumlike ions. The results are in generally good agreement with theoretical predictions. These results provide information unavailable from direct cross-section measurements, because they allow separation of different x-ray transitions from the same excited intermediate state.

The technique of sweeping the electron-beam energy while recording individual x-ray events has a much broader application. We plan to use it with a high-resolution crystal spectrometer to resolve dielectronic-recombination resonances to individual states. It may also be used for the measurement of two-photon decays, excited-state lifetimes, resonant excitation, and other phenomena.

ACKNOWLEDGMENTS

This research was performed under the auspices of the U.S. Department of Energy at the Lawrence Livermore National Laboratory under Contract No. W-7405-ENG-48.

* Present address: Lawrence Berkeley Laboratory, Berkeley, CA.

† Present address: Health Physics Department, Georgia Institute of Technology, Atlanta, GA.

[1] D. A. Knapp *et al.*, Phys. Rev. Lett. **62**, 2104 (1989).

[2] M. B. Schneider *et al.*, Phys. Rev. A **45**, R1291 (1992); M. B. Schneider *et al.*, in *Atomic Processes in Plasmas, Portland, Maine, 1991*, edited by Earl S. Marmar and James L. Terry, AIP Conf. Proc. No. 257 (AIP, New York, 1992), p. 26.

[3] R. E. Marrs *et al.*, Phys. Rev. Lett. **60**, 1715 (1988).

[4] M. A. Levine *et al.*, Nucl. Instrum. Methods B **43**, 431 (1989).

[5] I. G. Brown *et al.*, Appl. Phys. Lett. **49**, 1019 (1986).

[6] E. B. Salomon, J. H. Hubbell, and J. H. Scofield, At. Data Nucl. Data Tables **38**, 1 (1988).

[7] M. H. Chen, Phys. Rev. A **45**, 4604 (1992).

[8] S. Baker and R. D. Cousins, Nucl. Instrum. Methods **221**, 437 (1984).

[9] D. A. Knapp, PhD. thesis, Los Alamos National Laboratory Report No. LANL LA-10877-T (1986) (unpublished).

[10] M. H. Chen, Phys. Rev. A **33**, 994 (1986).

[11] K. LaGattuta and Y. Hahn, J. Phys. B **15**, 2101 (1982).